

The impact threshold of the aerosol radiative forcing on the boundary layer structure in the pollution region

Dandan Zhao^{†1,2}, Jinyuan Xin^{*†1,2,3}, Chongshui Gong⁴, Jiannong Quan⁵, Yuesi Wang^{1,2}, Guiqian Tang¹,

Yongxiang Ma¹, Lindong Dai¹, Xiaoyan Wu¹, Guangjing Liu¹, Yongjing Ma¹

1. State Key Laboratory of Atmospheric Boundary Layer Physics and Atmospheric Chemistry (LAPC),

Institute of Atmospheric Physics, Chinese Academy of Sciences, Beijing 100029, China

2. University of Chinese Academy of Sciences, Beijing 100049, China

3. Collaborative Innovation Center on Forecast and Evaluation of Meteorological Disasters, Nanjing

University of Information Science and Technology, Nanjing, 210044, China

4. Institute of Arid Meteorology, China Meteorological Administration, Lanzhou 730020, China

5. Institute of Urban Meteorology, Chinese Meteorological Administration, Beijing, China

(†) These authors contributed equally to this study.

(*) Correspondence to: Jinyuan Xin (xjy@mail.iap.ac.cn).

1 **Abstract:** Recently, there has been increasing interests in the relation between
2 particulate matter (PM) pollution and atmospheric boundary layer (ABL) structure.
3 This study aimed to qualitatively assess the interaction between PM and ABL
4 structure in essence and further quantitatively estimate aerosol radiative forcing
5 (ARF) effects on the ABL structure. Multi-period comparative analysis indicated that
6 the key to determining whether the haze outbreak or dissipation occurs is whether the
7 ABL structure satisfies the relevant conditions. However, the ABL structure change was
8 in turn highly related to the PM level and ARF. $|SFC-ATM|$ (SFC and ATM are the
9 ARFs at the surface and interior of the atmospheric column, respectively) is the absolute
10 difference between ground and atmosphere layer ARFs, and the $|SFC-ATM|$ change is
11 linearly related to the PM concentrations. However, the influence of ARF on the
12 boundary layer structure is nonlinear. With increasing $|SFC-ATM|$, the TKE level
13 exponentially decreased, which was notable in the lower layers/ABL but disappeared
14 at high altitudes/above the ABL. Moreover, the ARF effects threshold on the ABL
15 structure was determined for the first time, namely, once $|SFC-ATM|$ exceeded ~ 55
16 $W m^{-2}$, the ABL structure tends to quickly stabilize and thereafter change little with
17 increasing ARF. The threshold of the ARF effects on the boundary layer structure
18 could provide useful information for relevant atmospheric environment improvement
19 measures and policies, such as formulating phased air pollution control objectives.

20 **1. Introduction**

21 Most urban agglomerations in China, such as the North China Plain (NCP), have
22 suffered from poor air quality due to rapid increase in anthropogenic emissions.
23 Beijing, as the capital city of China and the principal city in the NCP area, has
24 frequently experienced severe and persistent haze events (Li et al., 2020; Wang et al.,
25 2018; Xu et al., 2019; Zhong et al., 2018). Previous studies have found that the
26 occurrence of PM pollution events in Beijing is not only inseparable from the serious
27 primary emissions and fast formation of secondary aerosols (An et al., 2019; Guo et
28 al., 2014; Li et al., 2017; Wang et al., 2014; Zheng et al., 2015; Wang et al., 2012), but
29 also largely affected by the ABL structure, which controls the diffusion, transmission,
30 and accumulation of pollutants (Han et al., 2009; Kotthaus and Grimmond, 2018;
31 Zheng et al., 2017). For instance, the PM concentration has a strong relationship with
32 the ABL height (ABLH) that determines the volume available for pollutant dispersion
33 (Haman et al., 2014; Schaefer et al., 2009; Su et al., 2018; Tang et al., 2016). In most
34 instances, heavy air pollution episodes occurred with persistent temperature
35 inversions (Xu et al., 2019; Zhong et al., 2017). Weak/calm winds are essential in the
36 long-term increase in air pollutants (Niu et al., 2010; Yang et al., 2016). Additionally,
37 severe air pollution is ever reported positively related to high atmospheric humidity,
38 one of the manifestations of stagnant ABL conditions (Tie et al., 2017; Petäjä et al.,
39 2016). Moreover, the feedback mechanism between the boundary layer structure and
40 aerosol loading during severe pollution events contributing to the outbreak of haze
41 pollution has been presented in previous studies (Huang et al., 2018; Liu et al., 2018;

42 Petäjä et al., 2016; Zhong et al., 2018b; Zhong et al., 2019; Zhao et al., 2019).

43 However, this topic has yet to be fully understood. More work is needed to
44 systematically study the interaction between ABL structure and PM pollution. Since
45 the surface directly influences the ABL, it is the only atmosphere layer characterized
46 by turbulent activities, while higher atmosphere layers are weakly turbulent because
47 of the strongly stable stratification (Munro, 2005). The ABL acts as a notable
48 turbulence buffer coupling the surface with the free atmosphere, and PM and gas
49 pollutants mainly suspended in the ABL are convectively spread throughout it. The
50 change of boundary layer structure determining the accumulation and diffusion of
51 pollutants in it could be largely linked to the difference of turbulent activity (Garratt et
52 al., 1992). Moreover, the change in solar radiation reaching the ground drives the
53 diurnal ABL evolution (Andrews, 2000). While the diurnal evolution of the
54 atmospheric thermodynamic status could be greatly affected considering a strong
55 aerosol direct radiation effect, namely strongly scattering radiation and absorbing
56 radiation (Dickerson et al., 1997; Liu et al., 2018; Huang et al., 2018; Stone et al.,
57 2008; Zhong et al., 2018a). As previous studies have reported that aerosol absorption
58 and scattering effects during severe air pollution notably enhance atmospheric
59 stability and suppress the boundary layer development (Barbaro et al., 2014; Ding et
60 al., 2016; Wilcox et al., 2016; Yu et al., 2002). Considering the aerosol radiative
61 forcing (ARF) is a critical parameter to quantify the aerosol direct radiation effect
62 (Gong et al., 2014; Li et al., 2018). The influence degree of ARF on the boundary
63 layer structure is still unclear, and thus quantitatively determining the effects of ARF

64 on the ABL structure is urgently needed.

65 In this study, we systematically analyzed the way the ABL interacts with PM
66 pollution via contrastive analysis of multiple haze episodes, based on not only specific
67 meteorological factors but also turbulent activity profiles and atmospheric stability
68 indicators. Meanwhile, taking the turbulent kinetic energy (TKE) and ARF as
69 important parameters, we further investigated the influence degree of the aerosol
70 direct radiation effect on the boundary layer structure. Besides, this paper analyzed
71 the interaction between the ABL structure and air pollution using high-resolution and
72 real-observation datasets, such as temperature and humidity profiles of microwave
73 radiometers, horizontal and vertical wind vector profiles of Doppler wind lidar,
74 ABLH, and aerosol backscattering coefficient profiles of ceilometers. Wind profile
75 lidar and microwave radiometers have the advantage of providing direct and
76 continuous observations of the boundary layer over long periods and can characterize
77 the ABL structure up to 2-3 km (Pichugina et al., 2019; Zhao et al., 2019),
78 compensating for the deficiencies of previous research.

79 **2. Data and methods**

80 Figure S1 shows the observation site of the Tower Branch of the Institute of
81 Atmospheric Physics (IAP), Chinese Academy of Sciences (39°58'N, 116°22'E;
82 altitude: 58 m) in Beijing and the sampling instruments in this study. The IAP site is a
83 typical urban Beijing site, and all the sampling instruments are placed at the same
84 location, and simultaneous monitoring is conducted. We conducted a two-month
85 measurement campaign of the PM concentration and aerosol optical depth (AOD) and

86 obtained vertical profiles of atmospheric parameters such as temperature, humidity,
87 wind vectors, atmospheric stability, and turbulent activity to better understand how
88 the boundary layer structure responds to the aerosol direct radiation effect.

89 The algorithm of SBDART (Santa Barbara DISORT Atmospheric Radiative
90 Transfer) (Levy et al., 2007) is the core model to calculate the aerosol radiative
91 forcing parameters. More information on the input parameters of SBDART were
92 presented in Table S2. A standard mid-latitude atmosphere is used in SBDART in
93 Beijing. AOD and Ångström Exponent (AE) at 550 nm were obtained from a sun-
94 photometer. Multiple sets of Single Scattering Albedo (SSA) and backscattering
95 coefficient were calculated based on MIE theory, and surface albedo & path radiation
96 were read from MODIS (MOD04), which is used to calculate radiative forcing at the
97 top of atmosphere (TOA). The TOA results were combined with MODIS
98 observations, and the result which has the lowest deviation are defined as the actual
99 parameters of aerosols, and this set of parameters would be used to calculate the
100 radiative forcing at the surface, top, and interior of the atmospheric column (Gong et
101 al., 2014; Lee et al, 2018; Xin et al., 2016). Hourly radiative forcing parameters,
102 including the ARF at the top, surface (SFC), and interior of the atmospheric column
103 (ATM) at an observation site in Beijing can be calculated based on this algorithm.
104 More detailed descriptions are provided in our previous work (Gong et al., 2014; Lee
105 et al, 2018; Xin et al., 2016).

106 Air temperature and relative and absolute humidity profiles were retrieved with a
107 microwave radiometer (after this referred to as MWR) (RPG-HATPRO-G5 0030109,

108 Germany). The MWR produces profiles with a resolution ranging from 10-30 m up to
109 0.5 km, profiles with a resolution ranging from 40-70 m between 0.5 and 2.5 km, and
110 profiles with a resolution ranging from 100-200 m from 2 to 10 km at a temporal
111 resolution of 1 s. More detailed information on the RPG-HATPRO-type instrument
112 can be found at <http://www.radiometer-physics.de> (last access: 4 June 2020).

113 Vertical wind speed and horizontal wind vector profiles were obtained by a 3D
114 Doppler wind lidar (Windcube 100s, Leosphere, France). The wind measurement
115 results have a spatial resolution ranging from 1-20 m up to 0.3 km and a spatial
116 resolution of 25 m from 0.3 to 3 km, at a temporal resolution of 5 s. More instrument
117 details can be found at www.leosphere.com (last access: 4 June 2020).

118 A ceilometer (CL51, Vaisala, Finland) was adopted to acquire atmospheric
119 backscattering coefficient (BSC) profiles. The CL51 ceilometer digitally receives the
120 return backscattering signal from 0 to 100 μ s and provides BSC profiles with a spatial
121 resolution of 10 m from the ground to a height of 15 km. The ABLH was further
122 identified by the sharp change in the BSC profile's negative gradient (Münkel et al.,
123 2007), and detailed information is reported in previous studies (Tang et al., 2015,
124 2016; Zhu et al., 2018).

125 A CIMEL sun-photometer (CE318, France), a multichannel, automatic sun-and-
126 sky scanning radiometer (Gregory, 2011), was used to observe the AOD, and the AOD
127 at 500 nm is adopted in this paper. The real-time hourly mean ground levels of PM_{2.5}
128 (particulate matter with aerodynamic diameter less than or equal to 2.5 μ m) and PM₁₀
129 (particulate matter with aerodynamic diameter less than or equal to 10 μ m) were

130 downloaded from the China National Environmental Monitoring Center (CNEMC)
131 (available at <http://106.37.208.233:20035/>, last access: 4 June 2020).

132 More atmospheric parameters regarding the boundary layer structure used in this
133 study are introduced in S1.

134 **3. Results and discussion**

135 **3.1. General haze episodes over Beijing in winter**

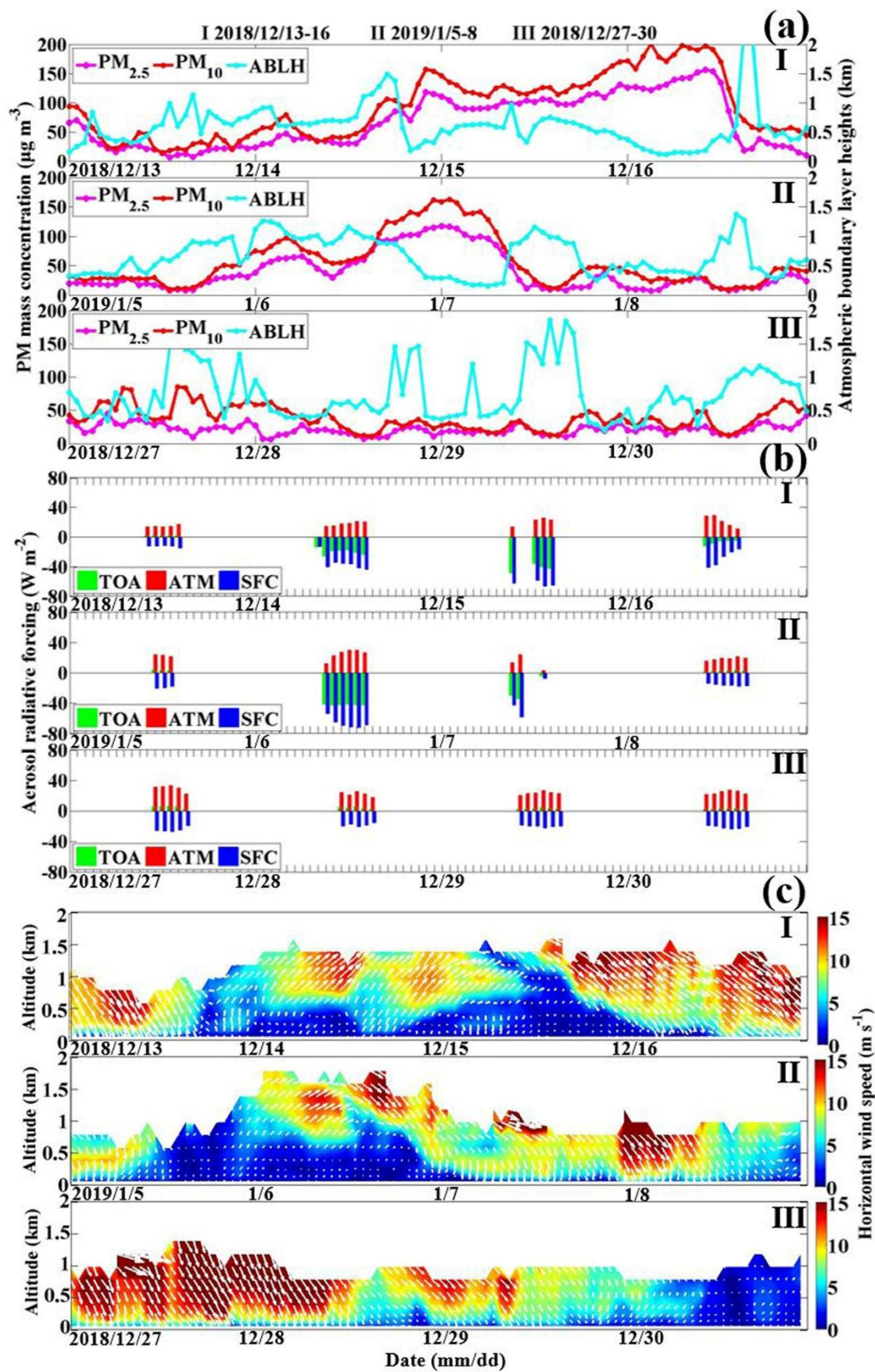
136 It is well known that severe air pollution episodes frequently occur in Beijing
137 during winter (Jin-Xiang, 2007; Zhang et al., 2017). Two-month PM concentration
138 data from Beijing in the winter of 2018 were collected. As expected, during this time,
139 Beijing experienced severe and frequent haze pollution episodes with two heavy
140 episodes in which the maximum hourly PM_{2.5} concentration reached \sim 200 $\mu\text{g m}^{-3}$ and
141 six moderate episodes in which the PM_{2.5} mass concentration ranged from \sim 100-150
142 $\mu\text{g m}^{-3}$ (Figure S2a).

143 Although the air pollution process is variable and complicated, it is worth stating
144 that Beijing's haze pollution in winter can be generally classified as two kinds of
145 patterns, as shown in Figure S2b. For all haze episodes ①-⑦, the PM_{2.5} mass
146 concentration slowly increased in the afternoon of the 1st day, followed by a
147 secondary maximum in the early morning and a maximum at midnight of the 2nd day.

148 In comparison to the processes of ④-⑦, where the PM_{2.5} mass concentration sharply
149 decreased to $<25 \mu\text{g m}^{-3}$ in the early morning of the 3rd day, during periods ①-③,
150 however, the highest PM_{2.5} mass concentration (\sim 100-200 $\mu\text{g m}^{-3}$) was observed on
151 the whole 3rd day, which disappeared on the 4th day. As previously reported,

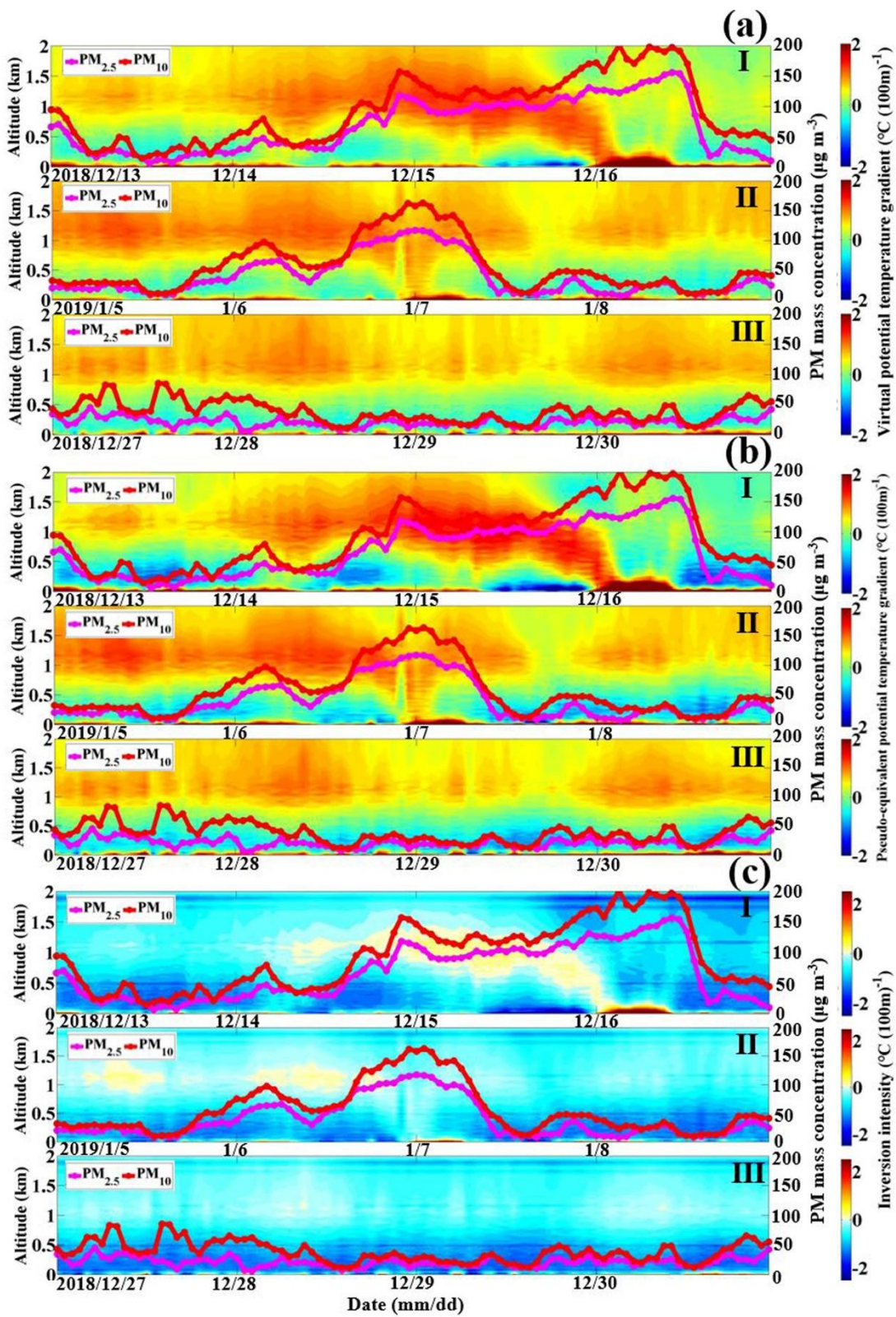
152 transport, chemical transformation and boundary layer structure (local meteorological
153 conditions) are central to determining the amount and type of pollutant loading.
154 Considering the equivalent emission and transport effects, the suspended particles in
155 ④-⑦ subjected to diffuse would be controlled by the atmospheric motion (wind and
156 turbulence) on the 3rd day. The particles during periods ①-③ continuing to
157 accumulate were therefore highly related to the specific ABL status. To investigate the
158 possible reasons for the different variation trends of haze episodes ①-③ and ④-⑦,
159 in the next section, we will mainly focus on the ABL structure (local meteorological
160 conditions) influences.

161 **3.2. Qualitative analysis of the interaction between particulate matter and**
162 **boundary layer structure**



163 Figure 1. Temporal evolution of (a) the PM mass concentration and atmospheric

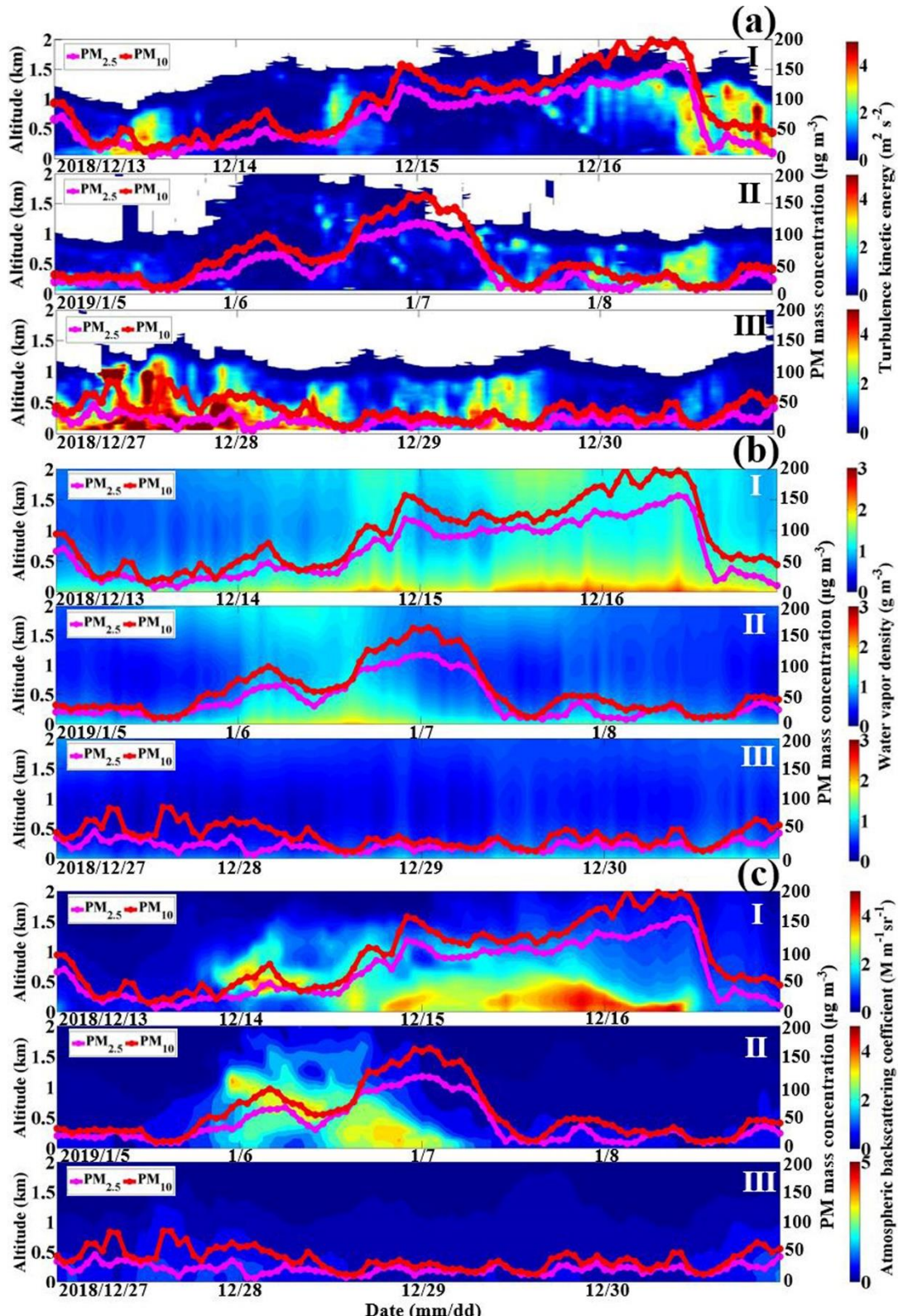
164 boundary layer height (PM_{2.5}: solid pink lines; PM₁₀: solid red lines; ABLH: solid
165 blue lines), (b) aerosol radiative forcing at the top (TOA; green bars), surface (SFC;
166 blue bars) and interior of the atmospheric column (ATM; red bars), and (c) horizontal
167 wind vector profiles (shaded colors: wind speeds; white arrows: wind vectors) during
168 the typical haze pollution episodes of I (2018/12/13-16) and II (2019/1/5-8) as well as
169 the typical clean period of III (2018/12/27-30).



170

171 Figure 2. Temporal variation in the vertical profiles of (a) the virtual potential
 172 temperature gradient ($\partial\theta_v/\partial z$), (b) pseudoequivalent potential temperature gradient
 173 ($\partial\theta_{se}/\partial z$) and (c) temperature inversion phenomenon (shaded colors: inversion

174 intensity) during the typical haze pollution episodes of I (2018/12/13-16) and II
 175 (2019/1/5-8) as well as the typical clean period of III (2018/12/27-30).



176

177 Figure 3. Temporal variation in the vertical profiles of (a) the turbulent activity

178 (shaded colors: TKE), (b) atmospheric humidity (shaded colors: vapor density), and
179 (c) vertical distribution of suspended particles (shaded colors: BSC) during the typical
180 haze pollution episodes of I (2018/12/13-16) and II (2019/1/5-8) as well as the typical
181 clean period of III (2018/12/27-30).

182 The haze episodes in winter in Beijing basically followed two different kinds of
183 variation patterns as described in the previous section. The specific reason for this
184 finding will be systematically analyzed in this section. To better illustrate the two
185 different haze patterns, a typical clean period will be considered a control. The typical
186 air pollution episodes I (E-I) (13-16 December 2018) and II (E-II) (5-8 January 2019),
187 as well as the typical clean episode III (E-III) (27-30 December 2018), are chosen as
188 examples for analysis.

189 *a. Similar change trends in the first two days*

190 Numerous studies have reported that PM's original explosive growth is caused
191 by pollution transport under southerly winds (Ma et al., 2017; Zhao et al., 2019;
192 Zhong et al., 2018). In this study, the action of southerly winds on the air pollution in
193 Beijing was presented more clearly as the Windcube 100s lidar obtained the
194 distribution of the horizontal wind vectors extending to heights of 1-1.5 km
195 (equivalent to the entire ABL) (Figure 1c). On the 1st day of E-I and E-II, the
196 atmosphere layer up to ~1 km in height was controlled by strong and clean north
197 winds, exactly like clean E-III. No pollution transport occurred, and the PM and ARF
198 levels were equivalent to those on a clean day (Figures 1a-b). The atmospheric
199 backscattering coefficients throughout the ABL during the three episodes only ranged

200 from \sim 0-1.5 $M\ m^{-1}\ sr^{-1}$ (Figure 3c). From the evening of the 1st day to the forenoon of
201 the 2nd day, strong southerly winds blew across Beijing during both E-I and E-II, with
202 the wind speed reaching \sim 5-15 $m\ s^{-1}$ at an atmosphere of about 0.5-1.5 km, while
203 north winds still dominated the ABL during clean E-III. Sensitive to the change in
204 wind direction from north to south, the PM concentration progressively increased
205 from a fairly low level to \sim 50 $\mu g\ m^{-3}$. Moreover, the BSCs sharply increased to \sim 3
206 $Mm^{-1}\ rd^{-1}$ and were concentrated at altitudes from \sim 0.5-1 km, which further stressed
207 the effects of southerly transport on the PM concentration's original growth over
208 Beijing. With prevailing winds originating from the wetter south, compared to the low
209 humidity during clean E-III, the air humidity in Beijing during this time also
210 increased, with the vapor density ranging from \sim 1.5-2 $g\ m^{-3}$ for both E-I and E-II
211 (Figure 3b).

212 At midnight of the 2nd day, the PM concentration reached its highest level with a
213 $PM_{2.5}$ (PM_{10}) concentration of \sim 110 (150) $\mu g\ m^{-3}$ during both E-I and E-II.
214 Meanwhile, the highest BSC values mainly occurred from the ground to a height of 1
215 km at this time, implying that a portion of the suspended particles was pushed down
216 to the near-surface. Before southerly wind transport occurred, the evolution of the
217 stability indicator ($\partial\theta_v/\partial z$; $\partial\theta_{se}/\partial z$) profiles during E-I and E-II was analogous to that
218 during clean E-III (Figures 2a-b). The stratification states at the different heights (0-1
219 km) were either unstable or neutral, with negative or zero $\partial\theta_v/\partial z$ values, respectively,
220 whereby no clear nor strong temperature inversion phenomenon occurred in the
221 boundary layer (Figure 2c). And the corresponding ABLHs were the same (Figure 1a).

222 However, the atmospheric stratification from ~0.5-1 km during E-I and from 0-1 km
223 during E-II became quite stable at night of the 2nd day, with positive values of $\partial\theta_{se}/\partial z$
224 and weak turbulent activity (TKE: $\sim 0 \text{ m}^2 \text{ s}^{-2}$) (Figure 3a). In contrast to an increased
225 ABLH during clean E-III, the ABLHs during E-I and E-II sharply decreased.
226 Considering strong aerosol scattering and absorbing radiation could affect the
227 temperature stratification (Li et al., 2010; Zhong et al., 2018a). With the elevated PM
228 level due to southerly transport during E-I and E-II, ARF increased as expected with
229 SFC (ATM) reaching ~ 40 (~ 20) W m^{-2} and ~ 75 (~ 30) W m^{-2} , respectively. Besides,
230 TOA has an analogous variation trend with SFC, increasing from relatively low
231 values to $\sim 20 \text{ W m}^{-2}$ and $\sim 45 \text{ W m}^{-2}$, respectively. Therefore, less radiation reached
232 the ground and more heated the atmosphere above the ground during E-I and E-II, and
233 in comparisons with clean E-III, the atmospheric stratification was altered and the
234 stability was thus increased at night. The suspended particles brought by southerly
235 transport originally occurring at high altitudes were restrained from vertically
236 spreading and gradually sank due to gravity and accumulated near the surface.

237 *b. Different change trends in the next two days*

238 It is salient to note that the haze evolution trends during E-I and E-II were
239 consistent so far, corresponding to a similar ABL structure. Nevertheless, the north
240 winds ($\sim 10\text{-}15 \text{ m s}^{-1}$) during E-II, which only blew above the ABL ($>1 \text{ km}$) at
241 midnight of the 2nd day, gradually spread downward and controlled the whole
242 boundary layer on the 3rd day. The wind field is critical concerning horizontal
243 dispersion in the boundary layer; thus, the strong, clean and dry north winds during E-

244 II greatly diffused the already accumulated particles first, where the PM_{2.5} mass
245 concentration decreased from ~100 to ~50 $\mu\text{g m}^{-3}$. The ARF obtained at 9:00 sharply
246 decreased compared to yesterday, and with solar radiation heating the ground in the
247 morning on the 3rd day, the development of daytime mixing layer eliminated the
248 previous night's temperature structure. The temperature stratification became similar
249 to that on clean E-III with a similar increase in ABLH. An unstable/neutral
250 atmospheric state with a TKE of $\sim 2 \text{ m}^2 \text{ s}^{-2}$ was also conducive to the vertical spread of
251 substances. In response, the PM concentration (BSC) and air humidity during E-II
252 gradually decreased with the convective boundary layer development and reached the
253 same level as those during clean E-III.

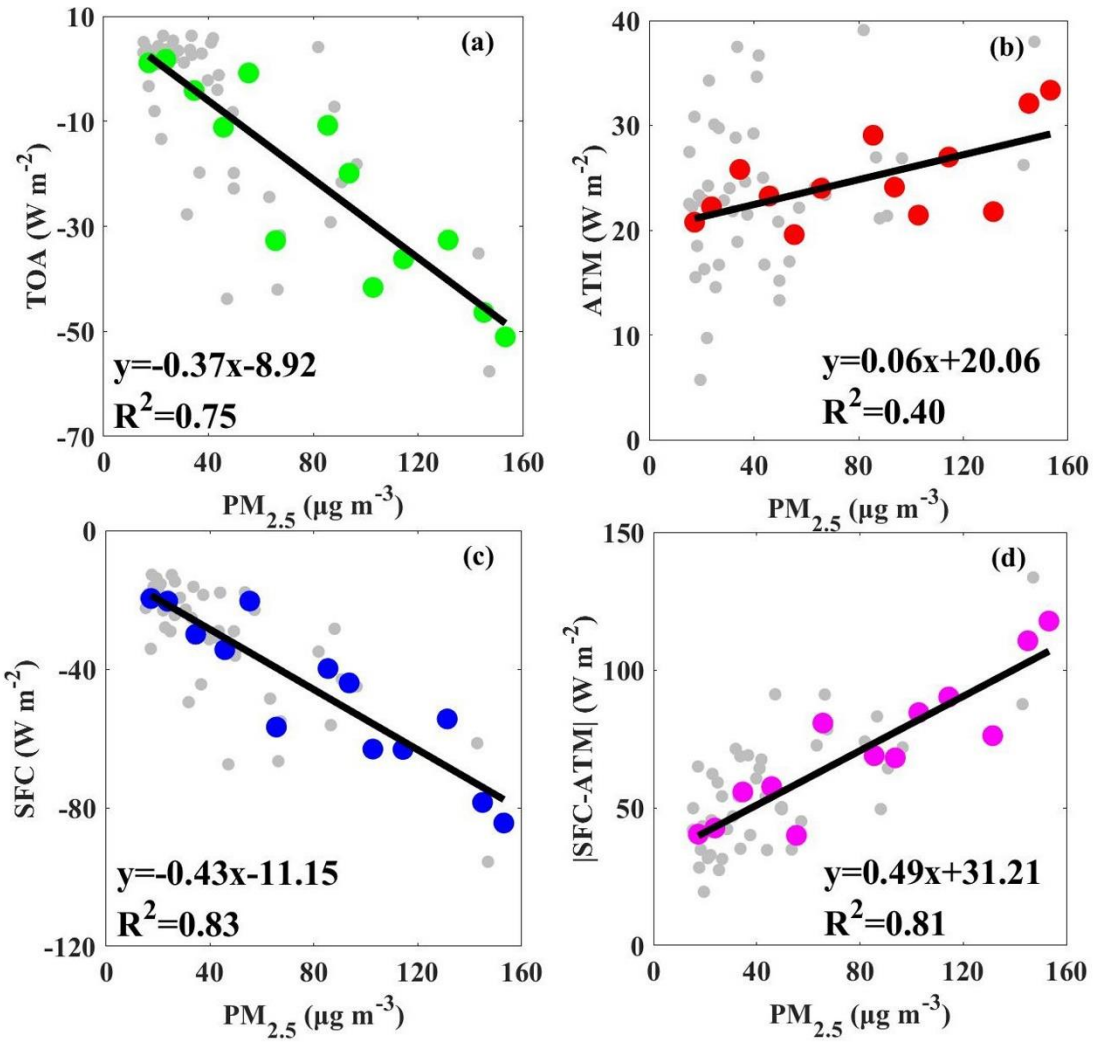
254 Different from E-II, in which clean and strong north winds in the 3rd daytime
255 contributed to the diffusion of previous night's stable stratification, there were still
256 south winds in E-I, which once filled the boundary layer on the 2nd day, gradually
257 decelerated over time from the ground to high altitudes. The atmosphere layer with
258 calm/light winds extended from the ground to the height of $\sim 1.0 \text{ km}$ in the 3rd
259 daytime and gradually down to the height of $\sim 0.2 \text{ km}$ at midnight and the forenoon of
260 the 4th day. Due to the maintaining high PM levels, SFC and TOA further increased,
261 up to $\sim 40 \text{ W m}^{-2}$ and $\sim 75 \text{ W m}^{-2}$, respectively, with ATM remaining high ($\sim 25 \text{ W m}^{-2}$), which facilitated the temperature inversion that lasted from the whole 3rd day to
262 the noon of the 4th day. As shown in Figure 2(a-c)-I, there was continue temperature
263 inversion structure from $\sim 0.5\text{-}1.0 \text{ km}$ altitude and the atmospheric stratification was
264 quite stable on the 3rd daytime and at midnight. Since the temperature inversion layer

266 acted as a lid at altitudes of ~0.5-1.0 km, downward momentum transport would be
267 blocked. Original south winds near the ground were constantly consumed by friction,
268 further explaining the lower atmosphere layer's calm/light winds. With quite strong
269 north winds started blowing at high altitude at the 3rd night and surface cooling
270 strengthening, the temperature inversion at ~0.5-1.0 km was gradually broke and
271 turned to ground-touching temperature inversion at 0-0.2 km altitude at midnight.
272 This abnormal temperature structure lasted till noon of the 4th day, mainly due to the
273 strong aerosol direct radiation effect of the pre-existing high PM level. As expected,
274 we can see the strong north winds above ~1.0 km at the 3rd night gradually extended
275 downward and eventually occurred above the ground-touching inversion in the
276 forenoon of the 4th day. Therefore, with calm/light winds and weak turbulent activity
277 below the temperature inversion in the 3rd day, the PM concentrated exactly below
278 the inversion lid (below ~0.5 km) and maintained high concentrations, as the BSC
279 distribution shows in Figure 3c-I. With strong ground-touching inversion of 0-0.2 km
280 altitude forming at midnight and the forenoon of the 4th day, the accumulated
281 particles near the surface were further inhibited right in the stable atmosphere layer
282 (below ~0.2 km). The same effect was exerted on the water vapor so as to the high air
283 humidity below the inversion lid at this time. Therefore, the pollutant layer was
284 compressed downward accompanied by intense heterogeneous hydrolysis reactions at
285 the moist particle surface (Zhang et al., 2008), thus resulting in the continue increase
286 of near-surface PM_{2.5} concentrations. At noon of the 4th day, the north winds further
287 accelerated with wind speed higher than ~15 m s⁻¹ and spread down to the whole

288 ABL, which promoted the horizontal and convective dispersion of pollutants and
289 water vapor, and the PM mass concentration, therefore, dropped to the same level as
290 that on clean E-III. With $\text{PM}_{2.5}$ sharply dropped from $\sim 150 \text{ } \mu\text{g m}^{-3}$ to $\sim 20 \text{ } \mu\text{g m}^{-3}$ in
291 four hours, the aerosol direct radiation effect was sensitive to PM changes and
292 gradually decreased from 10:00 to 14:00, reaching the same level as those on clean E-
293 III finally.

294 In this section, through a detailed contrastive analysis, we examined the potential
295 reasons for the occurrence of the two different patterns of haze pollution in winter in
296 Beijing. We found that the crucial point in determining whether the PM mass
297 concentration remained high or sharply decreased was related to whether the
298 boundary layer remained stable. The boundary layer stability was, in turn notably
299 linked to the PM mass concentration and aerosol direct radiation effect.

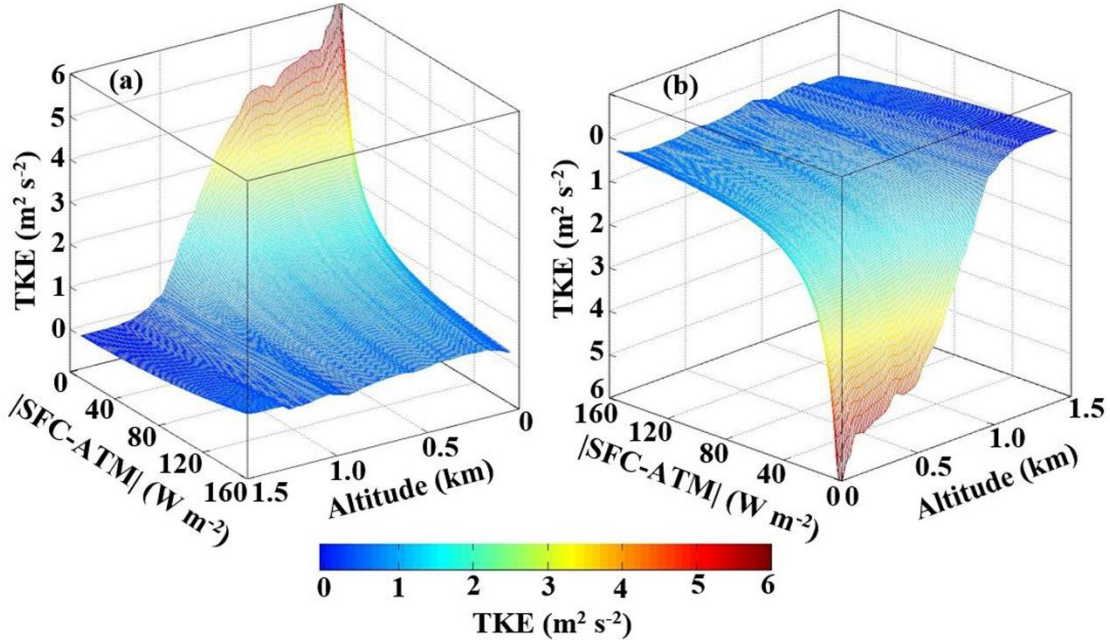
300 **3.3. Quantitative analysis of the effect of particulate matter on the boundary layer
301 structure**



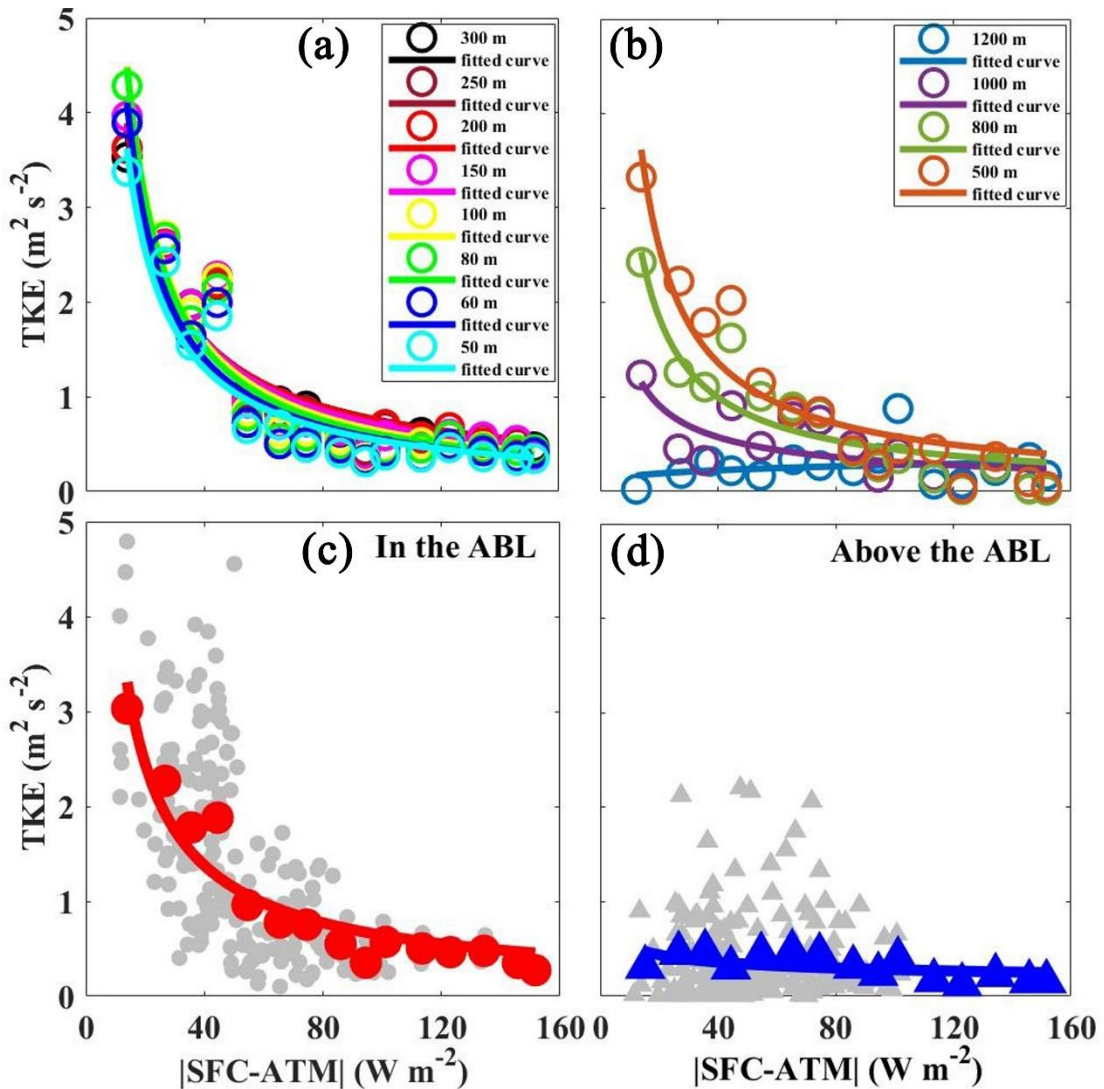
302

303 Figure 4. Scatter plots of the $\text{PM}_{2.5}$ mass concentration (x) versus aerosol radiative
 304 forcing at the top of the atmospheric column (TOA; y; a), the interior of the
 305 atmospheric column (ATM; y; b), and the surface (SFC; y; c) as well as the absolute
 306 difference of SFC and ATM ($|\text{SFC}-\text{ATM}|$; y; d), respectively (gray dots: daily data;
 307 other dots: mean data). (The daily data means daily mean values of TOA, ATM, SFC,
 308 and corresponding daily averaged $\text{PM}_{2.5}$ mass concentration from 27 November 2018
 309 to 25 January 2019 in Beijing. The mean $\text{PM}_{2.5}$ concentrations were obtained by
 310 averaging daily $\text{PM}_{2.5}$ concentrations at intervals of $10 \mu\text{g m}^{-3}$. The mean TOA, ATM,
 311 and SFC were obtained after the corresponding daily TOA, ATM, and SFC average,

312 respectively. For example, all daily PM_{2.5} concentrations greater than 40 $\mu\text{g m}^{-3}$ and
 313 less than 50 $\mu\text{g m}^{-3}$ were averaged as a mean PM_{2.5} concentration, and TOA values
 314 (ATM; SFC) corresponding to this daily PM_{2.5} concentration range were also averaged
 315 as a mean TOA (ATM; SFC)).



316
 317 Figure 5. 3-D plot of the fitting relationship of the absolute difference in aerosol
 318 radiative forcing between the surface and interior of the atmospheric column ($|\text{SFC-}$
 319 $\text{ATM}|$; x) and turbulence kinetic energy (TKE; z) at the different altitudes (y) ((a) and
 320 (b) present different perspectives).



321

322 Figure 6. Scatter plots of the mean absolute difference of the aerosol radiative forcing

323 at the surface and interior of the atmospheric column ($|SFC-ATM|$; x) versus the mean

324 turbulence kinetic energy (TKE; y) at the different altitudes (a; b). Scatter plots of

325 $|SFC-ATM|$ (x) versus TKE (y) in the ABL (c) and above the ABL (gray dots:

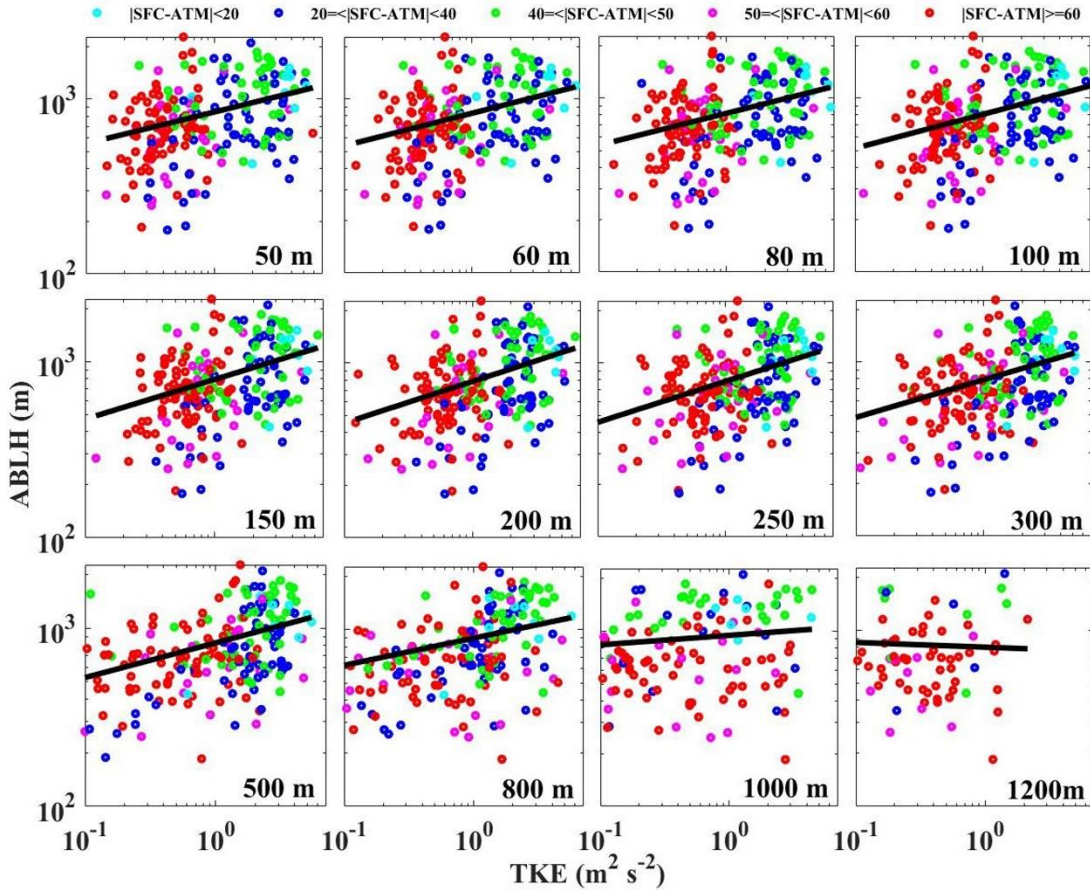
326 hourly data; other dots: mean data). The hourly data were collected over a two-month

327 period in Beijing from 27 November 2018 to 25 January 2019. (The hourly data

328 means hourly mean values of $|SFC-ATM|$ and corresponding hourly TKE. The mean

329 $|SFC-ATM|$ was obtained by averaging hourly $|SFC-ATM|$ at intervals of 10 W m^{-2} ,

330 then the mean TKE was obtained after the average of the corresponding hourly TKE.).



331

332 Figure 7. The atmospheric boundary layer height (ABLH; y) as a function of the
 333 turbulence kinetic energy (TKE; x) at the different altitudes and the aerosol direct
 334 radiation effect defined as $|\text{SFC-ATM}|$ (color code). The calculated hourly data used
 335 above are collected over two months in Beijing from 27 November 2018 to 25
 336 January 2019.

337 Based on the contrastive analysis in the previous section, it was clear that the
 338 ABL structure played a critical role in the maintenance and dissipation of air
 339 pollution. It appeared that the increase in atmospheric stability suppressed pollution
 340 diffusion under a weak turbulence activity and low ABLH. Water vapor also
 341 significantly accumulated to a relatively high level near the surface, further
 342 facilitating secondary aerosols' formation. The evolution of ABL stability essentially

343 occurred in response to the atmospheric temperature structure, as analyzed above,
344 which was influenced by the strong aerosol direct radiation effect (Andrews, 2000; Li
345 et al., 2010). The Archimedes buoyancy generated by the pulsating temperature field
346 in the gravity field exerted negative work on the turbulent pulsating field with a stable
347 ABL occurring. The turbulence served as a carrier for substance transport in the
348 boundary layer, such as water vapor, heat, and PM (Garratt et al., 1992). Thus, in the
349 following section, the ARF and TKE were chosen as the key parameters to examine
350 how PM affects and modifies the boundary layer structure.

351 Figure 4 shows the relationship between the PM concentration and ARF. As
352 shown in Figures 4a and 4c, TOA and SFC were proportional to the $PM_{2.5}$
353 concentration, respectively. With the increase in $PM_{2.5}$ concentration, elevated aerosol
354 loading near the surface would scatter more solar radiation back into outer space and
355 cause less solar radiation reaching the ground, corresponding to a cooling of the
356 surface and making negative SFC. TOA means the aerosol radiative forcing at the top
357 of the atmosphere column and is the sum of ATM and SFC. Considering that
358 anthropogenic aerosols are mostly scattering aerosols, the SFC forcing is generally
359 stronger than ATM, corresponding to a cooling of the earth-atmosphere system. The
360 TOA forcing was thus usually negative and had a similar trend with SFC. ATM,
361 driven by aerosol absorption effect and representing a warming effect of aerosols on
362 the atmosphere layer, exhibited a positive correlation with the $PM_{2.5}$ concentration
363 (see Figure 4b). These results demonstrated that a higher $PM_{2.5}$ concentration would
364 arouse a stronger ARF, further inhibiting solar radiation from reaching the ground and

365 heating the atmosphere layer more. $|SFC-ATM|$, defined as the absolute value of the
366 difference between SFC and ATM, represents aerosols' combined action on the solar
367 radiation reaching the aerosol layer and the ground. Larger values of $|SFC-ATM|$
368 indicate stronger aerosol scattering and/or absorption effects, further implying a more
369 significant temperature difference between the ground and the above atmosphere
370 layer. As expected, a positive linear correlation between $|SFC-ATM|$ and $PM_{2.5}$
371 concentration was found, as shown in Figure 4d.

372 As described in the above paragraph, there was a strong ARF under a high PM
373 loading, which markedly altered the atmospheric temperature structure, further
374 changing the ABL structure. It is necessary to determine the effect degree of ARF on
375 the boundary layer structure. Figure 5 shows the 3-D plots of the fitting relationship
376 between the hourly values of $|SFC-ATM|$ and TKE at the different altitudes. What
377 stood out in Figure 5a was the general decline in TKE concerning the growth of $|SFC-$
378 $ATM|$. With increasing $|SFC-ATM|$ value, the TKE value at the different altitudes
379 always decreased exponentially and approached zero below ~ 0.8 km. The notable
380 exponential function between TKE and $|SFC-ATM|$ explained that a strong ARF
381 would drastically change the boundary layer into highly stable conditions
382 characterized by a rather low TKE. The results above highlight the aerosol direct
383 radiation effect's nonnegligible impact on the boundary layer structure, especially
384 during the haze episode under a high aerosol loading with a strong ARF. It is well
385 known that a larger net negative/positive SFC/ATM arises a cooler/warmer
386 ground/atmosphere. An increase in $|SFC-ATM|$ implies the gradual intensification of

387 the ground cooling and/or atmosphere heating processes. Therefore, it changed the
388 atmospheric stratification into a gradually enhanced stable state, which was
389 characterized by increasingly weaker turbulence activities. Additionally, as shown in
390 Figure 5b, we can identify a critical point of the $|SFC-ATM|$ effects on TKE in the low
391 layers. In particular, TKE decreased with increasing $|SFC-ATM|$ and hardly changed
392 when $|SFC-ATM|$ exceeded the critical point.

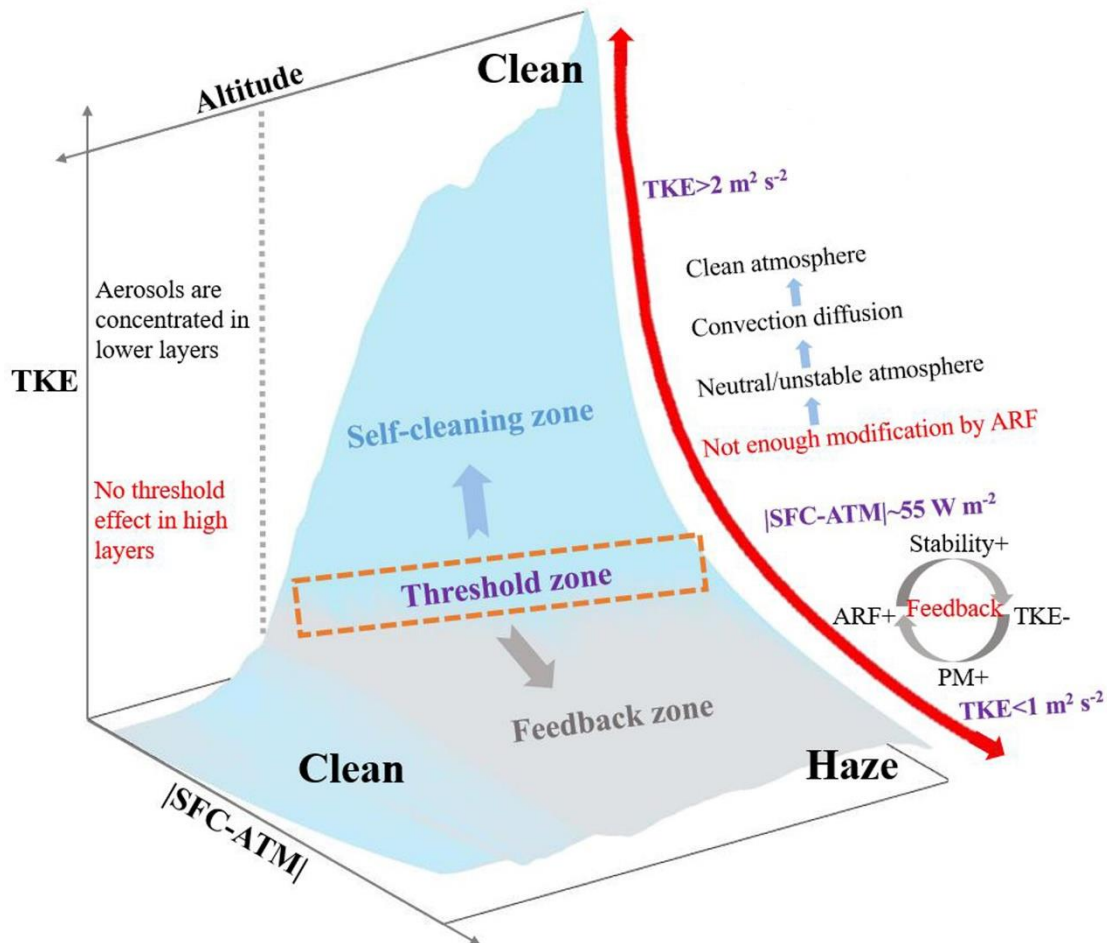
393 To define the critical point, we generated scatter plots of the average $|SFC-ATM|$
394 and TKE at different altitudes, as shown in Figures 6a-b. The scatter plots of the
395 unaveraged hourly data are shown in Figure S3, and the fitting functions are listed in
396 Table S1. Depending on the exponential curve's maximum curvature (Silvanus and
397 Gardner, 1998), a critical point should exist. With the mean TKE and $|SFC-ATM|$
398 values on the exponential curve, we found that once the aerosol direct radiation effect
399 defined by $|SFC-ATM|$ exceeded $50-60 \text{ W m}^{-2}$ (average of $\sim 55 \text{ W m}^{-2}$), the TKE
400 sharply decreased from $\sim 2 \text{ m}^2 \text{ s}^{-2}$ to lower than $1 \text{ m}^2 \text{ s}^{-2}$. This means that a high aerosol
401 loading with a $|SFC-ATM|$ value higher than $\sim 55 \text{ W m}^{-2}$ tends to change the boundary
402 layer from the unstable state to the extremely stable state in a short time, and further
403 increasing $|SFC-ATM|$ would barely modify the ABL structure. The average $|SFC-$
404 $ATM|$ value of $\sim 55 \text{ W m}^{-2}$ can be defined as the threshold of the ARF effects on the
405 ABL structure, which could provide useful information for relevant model
406 simulations, atmospheric environment improvement measures, and relevant policies.
407 Besides, as shown in Figures 5-6, the exponential relationship between TKE and
408 $|SFC-ATM|$ was notable in the low layers and gradually deteriorated with increasing

409 altitude. On average, the exponential relationship was notable in the ABL and almost
410 disappeared above the ABL (Figures 6c-d). Considering that aerosols are mainly
411 concentrated below the lower atmosphere, contributing the most to the SFC and ATM
412 forcing, which further confirmed that the considerable change in atmospheric
413 stratification caused by aerosols existed and mainly occurred in the lower layers.

414 The previous discussion shows that a strong aerosol direct radiation effect
415 markedly affected the turbulent activity and modified the boundary layer structure. As
416 many studies have reported, the ABLH is an important meteorological factor that
417 influences the vertical diffusion of atmospheric pollutants and water vapor (Stull,
418 1988; Robert and Aron, 1983). The following examines the relationship among the
419 turbulent activity, ARF, and ABLH to illustrate the change in ABLH in response to
420 ARF. Figure 7 shows the ABLH as a function of the TKE and $|SFC-ATM|$ at the
421 different altitudes. It was apparent that a positive correlation exists between TKE and
422 ABLH. As the turbulent activity became increasingly weaker, the corresponding
423 boundary layer height gradually decreased, responding to the gradual increase in
424 $|SFC-ATM|$. Similar to the relationship between the turbulent activity and aerosol
425 radiative effect, as shown in Figure 6, the relationship among these aspects was much
426 stronger below 300 m and almost disappeared above 800 m. This further addressed
427 the fact that the change in boundary layer height was attributed to the turbulence
428 activity variation stemming from the aerosol direct radiation effect.

429 Thus far, this section has demonstrated that the aerosol loading with aerosol
430 radiative effects impacted the turbulent activity, changed the boundary layer height,

431 and modified the boundary layer structure. On the other hand, it is now necessary to
432 explain how the renewed boundary layer structure modifies the PM_{2.5} concentration.
433 As shown in Figures S4a-b, the ABLH as an independent variable impact the ambient
434 water vapor in the ABL to some degree. There was a steady increase in the ambient
435 humidity with decreasing ABLH, where absolute humidity (AH) and relative
436 humidity (RH) were projected to decrease to ~ 3 g m⁻³ and $\sim 60\%$, respectively, with
437 the ABLH decreasing below ~ 500 m. With the increase in ambient humidity, a marked
438 rise in PM_{2.5} concentration occurred, as shown in Figures S4c-d. Once AH and RH
439 exceeded ~ 3 g m⁻³ and $\sim 60\%$, respectively, the PM_{2.5} concentration reached ~ 100 μg
440 m⁻³. The results above indicate that with a fairly low boundary layer height, water
441 vapor accumulated near the surface, and particles tended to hygroscopic grow,
442 resulting in secondary aerosol formation in a high-humidity environment, further
443 increasing the PM_{2.5} concentration. As shown in Figure S4e, with the level off of the
444 ABLH, the PM_{2.5} mass concentration increased exponentially and reached a high
445 value. The exponential relationship was similar to that between the ambient humidity
446 and ABLH, which revealed that the explosive growth of the PM_{2.5} concentration
447 under a low ABLH was largely driven by intense secondary aerosol formation and
448 hygroscopic growth at high ambient humidity.



449

450 Figure 8. Schematic diagram of the interaction between the aerosol radiative forcing (ARF)

451 and boundary layer structure ($|SFC-ATM|$: the mean absolute difference of the aerosol

452 radiative forcing at the surface and interior of the atmospheric column; TKE: the mean

453 turbulence kinetic energy).

454 **4. Conclusion**

455 By analyzing the two-month haze conditions in winter in Beijing, we found that

456 haze pollution basically underwent two different variation patterns, namely, the same

457 trends on the first two days, and on the next days, one haze pattern went through a

458 continuing outbreak, while the other haze pattern exhibited notable diffusion.

459 Considering equivalent emissions, this has raised important questions about whether

460 and how the local boundary layer structure impacted/caused this difference. The

461 results of a contrastive analysis qualitatively showed that the crucial point in
462 determining whether the PM concentration remained very high or sharply decreased
463 was largely related to whether the boundary layer structure (i.e., stability and TKE)
464 satisfied relevant conditions. As previous studies reported (Liu et al., 2018; Zhong et
465 al., 2018b; Zhong et al., 2019) and was confirmed in this paper, the extremely stable
466 stratification with positive $\partial\theta_{se}/\partial z$ values and a low TKE was the premise of the
467 outbreak of haze pollution. However, the change/state of the boundary layer structure
468 was, in turn, strongly linked to the PM mass concentration and ARF, and we further
469 quantitatively evaluated the effect of ARF on the boundary layer structure. Figure 8,
470 emerging from the previous observation analysis, is where ARF modifies the
471 boundary layer structure and aggravates haze pollution. The ARF effects on the
472 atmospheric stratification depend on the reduced radiation reaching the ground due to
473 aerosol scattering and absorbing radiation in the atmosphere (Dickerson et al., 1997;
474 Stone et al., 2008). Firstly, we found that a positive linear relationship between $|SFC-$
475 $ATM|$ and $PM_{2.5}$ concentration existed, which means the strong aerosol scattering
476 and/or absorption effect occurs during the heavy haze episodes and could arouse
477 significant temperature differences between the surface and the above atmosphere
478 layer. Secondly, previous studies revealed that black carbon solar absorption
479 suppresses turbulence near the surface (Wilcox et al., 2016); while we found that the
480 TKE value at the different altitudes always decreased exponentially with increasing
481 $|SFC-ATM|$, which was significant in the lower atmosphere layer. Moreover, the ARF
482 effects on turbulent activity were found significant in the boundary layer and

483 disappeared above the boundary layer, which also confirmed that the stronger ARF
484 from the aerosol layer would indeed change the boundary layer into the considerably
485 stable state characterized by a relatively low TKE. Thirdly, the ARF change is linear
486 due to the PM concentration; however, the influence of ARF on the boundary layer
487 structure is nonlinear. Based on the exponential relationship, the threshold of the ARF
488 effects on the boundary layer structure has been determined for the first time,
489 highlighting that once the ARF exceeded a specific value, the boundary layer structure
490 tends to quickly stabilize after that changed little with increasing ARF. This threshold
491 could provide useful information for relevant atmospheric environment improvement
492 measures and policies in Beijing. When the PM_{2.5} concentration is controlled with the
493 ARF below the threshold, the unstable atmosphere's self-purification capacity could
494 effectively dilute and diffuse pollutants. In contrast, when the PM_{2.5} concentration
495 increases with an ARF exceeding the threshold value, the boundary layer would
496 stabilize sharply, especially in the lower layers, aggravating haze pollution.

Data availability

The surface PM_{2.5} & PM₁₀ and other trace gases observation data used in this study can be accessed from <http://106.37.208.233:20035/> (last access: 4 June 2020). Other datasets can be accessed upon request to the corresponding author.

Author contribution

XJ designed the experiments and the research. ZD, GC, QJ, WY, TG, MY, DL, WX, LG, MY provided experimental assistance and analytical method. ZD and XJ analyzed the data and performed research. All authors commented on the manuscript.

Competing interests

The authors declare that they have no conflict of interest.

Acknowledgments

This study was supported by the Ministry of Science and Technology of China (grant number 2016YFC0202001), the CAS Strategic Priority Research Program (XDA23020301), and the National Natural Science Foundation of China (grant number 42061130215). The authors are thankful for the data support from the Ministry of Ecology and Environment of the People's Republic of China, the National Earth System Science Data Sharing Infrastructure, National Science and Technology Infrastructure of China (available at <http://www.geodata.cn>, last access: 4 June 2020).

References

An, Z., Huang, R.-J., Zhang, R., Tie, X., Li, G., Cao, J., Zhou, W., Shi, Z., Han, Y., Gu, Z., and Ji, Y.: Severe haze in northern China: A synergy of anthropogenic emissions and atmospheric processes, *Proc. Natl. Acad. Sci. U. S. A.*, 116, 8657-8666, <https://doi.org/10.1073/pnas.1900125116>, 2019.

Andrews, D. G.: *An Introduction to Atmospheric Physics*, Cambridge University Press, 2000.

Barbaro, E., Arellano, J., Ouwensloot, H., Schröter, J., Donovan, D., and Krol, M.: Aerosols in the convective boundary layer: Shortwave radiation effects on the coupled land-atmosphere system, *J. Geophys. Res.: Atmos.*, 119, 5845–5863, <https://doi.org/10.1002/2013JD021237>, 2014.

Dickerson, R. R., Kondragunta, S., Stenchikov, G., Civerolo, K. L., Doddridge, B. G., and Holben, B. N.: The impact of aerosols on solar ultraviolet radiation and photochemical smog, *Science* (New York, N.Y.), 278, 827-830, <https://doi.org/10.1126/science.278.5339.827>, 1997.

Garratt, J. R., Dessler, A. J., Houghton, J. T., and Rycroft, M. J.: The atmospheric boundary layer, 1992.

Ding, A., Huang, X., Nie, W., Sun, J., Kerminen, V.-M., Petäjä, T., Su, H., Cheng, Y., Yang, X., Wang, M., Chi, X., Wang, J., Virkkula, A., Guo, W., Yuan, J., Wang, S., Zhang, R., Wu, Y., Song, Y., Zhu, T., Zilitinkevich, S., and Kulmala, M.: Enhanced haze pollution by black carbon in megacities in China, *Geophys. Res. Lett.*, 43, 2873–2879, <https://doi.org/10.1002/2016GL067745>, 2016.

Gong, C., Xin, J., Wang, S., Wang, Y., Wang, P., Wang, L., and Li, P.: The aerosol direct radiative forcing over the Beijing metropolitan area from 2004 to 2011, *J. Aerosol Sci.*, 69, 62-70, <https://doi.org/10.1016/j.jaerosci.2013.12.007>, 2014.

Gregory, L.: *Cimel Sun-photometer (CSPHOT) Handbook*, 2011.

Guo, S., Hu, M., Zamora, M. L., Peng, J., Shang, D., Zheng, J., Du, Z., Wu, Z., Shao, M., Zeng, L., Molina, M. J., and Zhang, R.: Elucidating severe urban haze formation in China, *Proc. Natl. Acad. Sci. U. S. A.*, 111, 17373-17378,

https://doi.org/10.1073/pnas.1419604111, 2014.

Haman, C. L., Couzo, E., Flynn, J. H., Vizuete, W., Heffron, B., and Lefer, B. L.: Relationship between boundary layer heights and growth rates with ground-level ozone in Houston, Texas, *J. Geophys. Res.: Atmos.*, 119, 6230-6245, https://doi.org/10.1002/2013jd020473, 2014.

Han, S., Bian, H., Tie, X., Xie, Y., Sun, M., and Liu, A.: Impact of nocturnal planetary boundary layer on urban air pollutants: Measurements from a 250-m tower over Tianjin, China, *J. Hazard. Mater.*, 162, 264-269, https://doi.org/10.1016/j.jhazmat.2008.05.056, 2009.

Hua, Y., Wang, S., Wang, J., Jiang, J., Zhang, T., Song, Y., Kang, L., Zhou, W., Cai, R., Wu, D., Fan, S., Wang, T., Tang, X., Wei, Q., Sun, F., and Xiao, Z.: Investigating the impact of regional transport on PM2.5 formation using vertical observation during APEC 2014 Summit in Beijing, *Atmos. Chem. Phys.*, 16, 15451-15460, https://doi.org/10.5194/acp-16-15451-2016, 2016.

Huang, X., Wang, Z., and Ding, A.: Impact of Aerosol-PBL Interaction on Haze Pollution: Multiyear Observational Evidences in North China, *Geophys. Res. Lett.*, 45, 8596-8603, https://doi.org/10.1029/2018gl079239, 2018.

Jin-Xiang, L. I.: The Characteristics and Cause Analysis of Heavy-Air-Pollution in Autumn and Winter in Beijing, *Environ. Monit. China*, 2007.

Kotthaus, S., and Grimmond, C. S. B.: Atmospheric boundary-layer characteristics from ceilometer measurements. Part 1: A new method to track mixed layer height and classify clouds, *Q. J. R. Meteorol. Soc.*, 144, 1525-1538, https://doi.org/10.1002/qj.3299, 2018.

Lee K., Li Z., Wong M., Xin J., Wang Y., Hao W., and Zhao F.: Aerosol single scattering albedo estimated across China from a combination of ground and satellite measurements, *J. Geophys. Res.: Atmos.*, 112(D22), https://doi.org/10.1029/2007JD009077, 2007.

Levy, R. C., Remer, L. A., and Dubovik, O.: Global aerosol optical properties and application to Moderate Resolution Imaging Spectroradiometer aerosol retrieval

over land, *J. Geophys. Res.: Atmos.*, 112, <https://doi.org/10.1029/2006jd007815>, 2007.

Li, G., Bei, N., Cao, J., Huang, R., Wu, J., Feng, T., Wang, Y., Liu, S., Zhang, Q., Tie, X., and Molina, L. T.: A possible pathway for rapid growth of sulfate during haze days in China, *Atmos. Chem. Phys.*, 17, 3301-3316, <https://doi.org/10.5194/acp-17-3301-2017>, 2017.

Li, M., Wang, L., Liu, J., Gao, W., Song, T., Sun, Y., Li, L., Li, X., Wang, Y., Liu, L., Daellenbach, K. R., Paasonen, P. J., Kerminen, V.-M., Kulmala, M., and Wang, Y.: Exploring the regional pollution characteristics and meteorological formation mechanism of PM_{2.5} in North China during 2013-2017, *Environ. Int.*, 134, <https://doi.org/10.1016/j.envint.2019.105283>, 2020.

Li, Z., Lee, K.-H., Wang, Y., Xin, J., and Hao, W.-M.: First observation-based estimates of cloud-free aerosol radiative forcing across China, *J. Geophys. Res.: Atmos.*, 115, <https://doi.org/10.1029/2009jd013306>, 2010.

Liu, Q., Jia, X., Quan, J., Li, J., Li, X., Wu, Y., Chen, D., Wang, Z., and Liu, Y.: New positive feedback mechanism between boundary layer meteorology and secondary aerosol formation during severe haze events, *Sci. Rep.*, 8, <https://doi.org/10.1038/s41598-018-24366-3>, 2018.

Liu, T. T., Gong, S., Meng, Y., Qi, C. Z., and Hong, L. L.: Contributions of meteorology and emission to the 2015 winter severe haze pollution episodes in Northern China, *Atmos. Chem. Phys.*, 17, 1-17, <https://doi.org/10.5194/acp-2016-204>, 2016.

Münkel, C., Eresmaa, N., Rasanen, J., and Karppinen, A.: Retrieval of mixing height and dust concentration with lidar ceilometer, *Bound.-Layer Meteorol.*, 124, 117-128, <https://doi.org/10.1007/s10546-006-9103-3>, 2007.

Ma, Q., Wu, Y., Zhang, D., Wang, X., and Zhang, R.: Roles of regional transport and heterogeneous reactions in the PM_{2.5} increase during winter haze episodes in Beijing, *Sci. Total Environ.*, 599-600, 246-253, <https://doi.org/10.1016/j.scitotenv.2017.04.193>, 2017.

Miao, Y., Guo, J., Liu, S., Zhao, C., Li, X., Zhang, G., Wei, W., and Ma, Y.: Impacts of

synoptic condition and planetary boundary layer structure on the trans-boundary aerosol transport from Beijing-Tianjin-Hebei region to northeast China, *Atmos. Environ.*, 181, 1-11, <https://doi.org/10.1016/j.atmosenv.2018.03.005>, 2018.

Munro, D. S.: *Boundary Layer Climatology*, 2005.

Niu, F., Li, Z., Li, C., Lee, K.-H., and Wang, M.: Increase of wintertime fog in China: Potential impacts of weakening of the Eastern Asian monsoon circulation and increasing aerosol loading, *J. Geophys. Res.: Atmos.*, 115, <https://doi.org/10.1029/2009jd013484>, 2010.

Petaja, T., Jarvi, L., Kerminen, V. M., Ding, A. J., Sun, J. N., Nie, W., Kujansuu, J., Virkkula, A., Yang, X. Q., Fu, C. B., Zilitinkevich, S., and Kulmala, M.: Enhanced air pollution via aerosol-boundary layer feedback in China, *Sci. Rep.*, 6, <https://doi.org/10.1038/srep18998>, 2016.

Pichugina, Y. L., Banta, R. M., Bonin, T., Brewer, W. A., Choukulkar, A., McCarty, B. J., Baidar, S., Draxl, C., Fernando, H. J. S., Kenyon, J., Krishnamurthy, R., Marquis, M., Olson, J., Sharp, J., and Stoelinga, M.: Spatial Variability of Winds and HRRR-NCEP Model Error Statistics at Three Doppler-Lidar Sites in the Wind-Energy Generation Region of the Columbia River Basin, *J. Appl. Meteorol. Climatol.*, 58, 1633-1656, <https://doi.org/10.1175/jamc-d-18-0244.1>, 2019.

Quan, J., Gao, Y., Zhang, Q., Tie, X., Cao, J., Han, S., Meng, J., Chen, P., and Zhao, D.: Evolution of planetary boundary layer under different weather conditions, and its impact on aerosol concentrations, *Particuology*, 11, 34-40, <https://doi.org/10.1016/j.partic.2012.04.005>, 2013.

Robert, and Aron: Mixing height—an inconsistent indicator of potential air pollution concentrations, *Atmos. Environ.*, 17, 2193-2197, [https://doi.org/10.1016/0004-6981\(83\)90215-9](https://doi.org/10.1016/0004-6981(83)90215-9), 1983.

Schaefer, K., Wang, Y., Muenkel, C., Emeis, S., Xin, J., Tang, G., Norra, S., Schleicher, N., Vogt, J., and Suppan, P.: Evaluation of continuous ceilometer-based mixing layer heights and correlations with PM_{2.5} concentrations in Beijing, in: *Remote Sensing of Clouds and the Atmosphere Xiv*, edited by: Picard, R. H., Schaefer, K.,

Comeron, A., Kassianov, E., and Mertens, C. J., Proceedings of SPIE, 2009.

Silvanus, P. T. F. R. S., and Gardner, M.: A Little More about Curvature of Curves, Calculus Made Easy, 249-262, https://doi.org/10.1007/978-1-349-15058-8_25, 1998.

Stone, R. S., Anderson, G. P., Shettle, E. P., Andrews, E., Loukachine, K., Dutton, E. G., Schaaf, C., and Roman, M. O., III: Radiative impact of boreal smoke in the Arctic: Observed and modeled, *J. Geophys. Res.: Atmos.*, 113, <https://doi.org/10.1029/2007jd009657>, 2008.

Stull, R. B.: An Introduction to Boundary Layer Meteorology, 1988.

Su, T., Li, Z., and Kahn, R.: Relationships between the planetary boundary layer height and surface pollutants derived from lidar observations over China: regional pattern and influencing factors, *Atmos. Chem. Phys.*, 18, 15921-15935, <https://doi.org/10.5194/acp-18-15921-2018>, 2018.

Tang, G., Zhu, X., Hu, B., Xin, J., Wang, L., Münkel, C., Mao, G., and Wang, Y.: Impact of emission controls on air quality in Beijing during APEC 2014: lidar ceilometer observations, *Atmos. Chem. Phys.*, 15, 12667–12680, <https://doi.org/10.5194/acp-15-12667-2015>, 2015.

Tang, G., Zhang, J., Zhu, X., Song, T., Muenkel, C., Hu, B., Schaefer, K., Liu, Z., Zhang, J., Wang, L., Xin, J., Suppan, P., and Wang, Y.: Mixing layer height and its implications for air pollution over Beijing, China, *Atmos. Chem. Phys.*, 16, 2459-2475, <https://doi.org/10.5194/acp-16-2459-2016>, 2016.

Tie, X., Huang, R.-J., Cao, J., Zhang, Q., Cheng, Y., Su, H., Chang, D., Poeschl, U., Hoffmann, T., Dusek, U., Li, G., Worsnop, D. R., and O'Dowd, C. D.: Severe Pollution in China Amplified by Atmospheric Moisture, *Sci. Rep.*, 7, <https://doi.org/10.1038/s41598-017-15909-1>, 2017.

Wang, J. Z., Gong, S. L., Zhang, X. Y., Yang, Y. Q., Hou, Q., Zhou, C. H., and Wang, Y. Q.: A Parameterized Method for Air-Quality Diagnosis and Its Applications, *Adv. Meteorol.*, <https://doi.org/10.1155/2012/238589>, 2012.

Wang, X., Wei, W., Cheng, S., Li, J., Zhang, H., and Lv, Z.: Characteristics and

classification of PM 2.5 pollution episodes in Beijing from 2013 to 2015, *Sci. Total Environ.*, 612, 170-179, <https://doi.org/10.1016/j.scitotenv.2017.08.206>, 2018.

Wang, Y., Yao, L., Wang, L., Liu, Z., Ji, D., Tang, G., Zhang, J., Sun, Y., Hu, B., and Xin, J.: Mechanism for the formation of the January 2013 heavy haze pollution episode over central and eastern China, *Sci. China-Earth Sci.*, 57, 14-25, <https://doi.org/10.1007/s11430-013-4773-4>, 2014.

Wilcox, E. M., Thomas, R. M., Praveen, P. S., Pistone, K., Bender, F. A. M., and Ramanathan, V.: Black carbon solar absorption suppresses turbulence in the atmospheric boundary layer, *Proc. Natl. Acad. Sci. U. S. A.*, 113, 11794-11799, <https://doi.org/10.1073/pnas.1525746113>, 2016.

Xin, J., Gong, C., Wang, S., and Wang, Y.: Aerosol direct radiative forcing in desert and semi-desert regions of northwestern China, *Atmos. Res.*, 171, 56-65, <https://doi.org/10.1016/j.atmosres.2015.12.004>, 2016.

Xu, T., Song, Y., Liu, M., Cai, X., Zhang, H., Guo, J., and Zhu, T.: Temperature inversions in severe polluted days derived from radiosonde data in North China from 2011 to 2016, *Sci. Total Environ.*, 647, 1011-1020, <https://doi.org/10.1016/j.scitotenv.2018.08.088>, 2019.

Yu, H., Liu, S., and Dickinson, R.: Radiative effects of aerosols on the evolution of the atmospheric boundary layer, *J. Geophys. Res.*, 107(D12), 1, 4142-14, <https://doi.org/10.1029/2001JD000754>, 2002.

Yang, Y., Liao, H., and Lou, S.: Increase in winter haze over eastern China in recent decades: Roles of variations in meteorological parameters and anthropogenic emissions, *J. Geophys. Res.: Atmos.*, 121, 13050-13065, <https://doi.org/10.1002/2016jd025136>, 2016.

Zhang, Q., Ma, Q., Zhao, B., Liu, X., Wang, Y., Jia, B., and Zhang, X.: Winter haze over North China Plain from 2009 to 2016: Influence of emission and meteorology, *Environ. Pollut.*, 242, 1308-1318, <https://doi.org/10.1016/j.envpol.2018.08.019>, 2018.

Zhang, R., Khalizov, A. F., Pagels, J., Zhang, D., Xue, H., and McMurry, P. H.:

Variability in morphology, hygroscopicity, and optical properties of soot aerosols during atmospheric processing, Proc. Natl. Acad. Sci. U. S. A., 105, 10291-10296, <https://doi.org/10.1073/pnas.0804860105>, 2008.

Zhang, Z., Zhang, X., Zhang, Y., Wang, Y., Zhou, H., Shen, X., Che, H., Sun, J., and Zhang, L.: Characteristics of chemical composition and role of meteorological factors during heavy aerosol pollution episodes in northern Beijing area in autumn and winter of 2015, Tellus B, 69, <https://doi.org/10.1080/16000889.2017.1347484>, 2017.

Zhao, D., Xin, J., Gong, C., Quan, J., Liu, G., Zhao, W., Wang, Y., Liu, Z., and Song, T.: The formation mechanism of air pollution episodes in Beijing city: Insights into the measured feedback between aerosol radiative forcing and the atmospheric boundary layer stability, Sci. Total Environ., 692, 371-381, <https://doi.org/10.1016/j.scitotenv.2019.07.255>, 2019.

Zheng, C., Zhao, C., Zhu, Y., Wang, Y., Shi, X., Wu, X., Chen, T., Wu, F., and Qiu, Y.: Analysis of influential factors for the relationship between PM_{2.5} and AOD in Beijing, Atmos. Chem. Phys., 17, 13473-13489, <https://doi.org/10.5194/acp-17-13473-2017>, 2017.

Zheng, G. J., Duan, F. K., Su, H., Ma, Y. L., Cheng, Y., Zheng, B., Zhang, Q., Huang, T., Kimoto, T., Chang, D., Poeschl, U., Cheng, Y. F., and He, K. B.: Exploring the severe winter haze in Beijing: the impact of synoptic weather, regional transport and heterogeneous reactions, Atmos. Chem. Phys., 15, 2969-2983, <https://doi.org/10.5194/acp-15-2969-2015>, 2015.

Zhong, J., Zhang, X., Wang, Y., Sun, J., Zhang, Y., Wang, J., Tan, K., Shen, X., Che, H., Zhang, L., Zhang, Z., Qi, X., Zhao, H., Ren, S., and Li, Y.: Relative Contributions of Boundary-Layer Meteorological Factors to the Explosive Growth of PM_{2.5} during the Red-Alert Heavy Pollution Episodes in Beijing in December 2016, J. Meteorol. Res., 31, 809-819, <https://doi.org/10.1007/s13351-017-7088-0>, 2017.

Zhong, J., Zhang, X., Wang, Y., Liu, C., and Dong, Y.: Heavy aerosol pollution episodes in winter Beijing enhanced by radiative cooling effects of aerosols, Atmos. Res.,

209, 59-64, <https://doi.org/10.1016/j.atmosres.2018.03.011>, 2018a.

Zhong, J., Zhang, X., Dong, Y., Wang, Y., Liu, C., Wang, J., Zhang, Y., and Che, H.: Feedback effects of boundary-layer meteorological factors on cumulative explosive growth of PM2.5 during winter heavy pollution episodes in Beijing from 2013 to 2016, *Atmos. Chem. Phys.*, 18, 247–258, <https://doi.org/10.5194/acp-18-247-2018>, 2018b.

Zhong, J., Zhang, X., Wang, Y., Wang, J., Shen, X., Zhang, H., Wang, T., Xie, Z., Liu, C., Zhang, H., Zhao, T., Sun, J., Fan, S., Gao, Z., Li, Y., and Wang, L.: The two-way feedback mechanism between unfavorable meteorological conditions and cumulative aerosol pollution in various haze regions of China, *Atmos. Chem. Phys.*, 19, 3287–3306, <https://doi.org/10.5194/acp-19-3287-2019>, 2019.

Zhu, X., Tang, G., Lv, F., Hu, B., Cheng, M., Muenkel, C., Schafer, K., Xin, J., An, X., Wang, G., Li, X., and Wang, Y.: The spatial representativeness of mixing layer height observations in the North China Plain, *Atmos. Res.*, 209, 204-211, <https://doi.org/10.1016/j.atmosres.2018.03.019>, 2018.